HONG-PYO KIM[1*], JONG-YEON LEE[1], SUNG-HWAN CHO[1], MIN-JAE CHOI[1], SUNG-WOO KIM[1],
HYUNG-HA JIN[1], DONG-JIN KIM[1], SEOUNG-SIK HWANG[1], YUN-SOO LIM[1]

FRACTOGRAPHY OF STRESS CORROSION CRACKING OF 20% COLD WORKED TYPE 304 H STAINLESS STEEL CONTAINING δ-FERRITE IN OXIDIZING PRIMARY WATER

Fractography of stress corrosion cracking (SCC) of 20% cold worked Type 304 H stainless steel containing δ-ferrite was studied using a compact tension (CT) specimen in oxidizing primary water with a scanning electron microscope (SEM) and electron back scattered diffraction (EBSD). The stress corrosion crack propagated mostly in transgranular stress corrosion cracking (TGSCC) mode and sometimes in intergranular stress corrosion cracking (IGSCC) mode. TGSCC paths were along the {111} plane with both high resolved shear stress and high resolved tensile stress. IGSCC preferentially propagated along the grain boundary perpendicular to the loading axis. The findings in this work suggest that TGSCC proceeds through formation of a weakening zone at the head of the crack tip by interaction of slip and corrosion and then cracking of the weakened zone by tensile stress.

Keywords: Type 304 H stainless steel; stress corrosion cracking; fractography; primary water

1. Introduction

Type 304 stainless steel is widely used in primary system of pressurized water reactor because it has excellent corrosion resistance in primary water. However, it may be subject to stress corrosion cracking (SCC) in neutron irradiation [1], an oxidizing environment [2] or with prolonged usage in normal primary water [3]. Primary component materials in a pressurized water reactor (PWR) are exposed to a reducing environment to prevent SCC. However, materials in the occluded zone of the upper head of the reactor may be exposed to an oxidizing environment because air trapped in the occluded zone during refueling stage may not easily be removed immediately during the subsequent operation stage. The oxidizing environment significantly enhances SCC of stainless steel [2]. SCC of stainless steel propagates mostly in the intergranular mode [4] and sometimes in the transgranular mode [5] in primary water of a PWR. Cold work significantly enhances TGSCC in an oxidizing environment [6]. However, fractographic features of the TGSCC in oxidizing high temperature water have not been fully identified.

The general fractographic features of TGSCC are now well known [9-15] for stainless steel in a boiling MgCl$_2$ solution. The fracture surfaces generally exhibit highly crystallographic cleavage-like features. River lines on the fracture surfaces make it possible to determine the microscopic crack propagation direction in grain and from grain to grain, much as in the case of cleavage crack propagation [9]. Many papers dealing with crystallographic features of TGSCC of 304 stainless steel in a boiling MgCl$_2$ solution reported that fracture facets of TGSCC are low index planes. However, the low index planes reported varied among researchers from {100} [10-12] to {110} [13] to {111} [14]. Crystallographic features of TGSCC were studied with etch pitting, photogrammetry and the electron channeling technique. Mukai et al. [10] found that the facets generally were {100} and the crack growth direction was <110>. Meletis and Hochmann [11, 12] found that the facets were predominantly {100} plane with some {110} facets also present. Liu et al. [13] showed that the facets were {110} and {211}. Nakayama and Takano [14] found that fracture facets were {100} plane and {111} planes. The difference in fracture facets of TGSCC of 304 stainless steel in a boiling MgCl$_2$ solution suggests that variation in chemical composition, microstructure, cold work, stress or environment may change fracture facets from {100} to {110} to {111}.

The purpose of this study was to identify the fractographic features of TGSCC in Type 304 H stainless steel containing δ-ferrite in oxidizing primary water in a PWR.

1   KOREA ATOMIC ENERGY RESEARCH INSTITUTE, MATERIALS SAFETY RESEARCH DIVISION, 989-111 DAEDEOK-DAERO, YUSEONG-GU, DAEJEON, 305-353, REPUBLIC OF KOREA

*   Corresponding author: hpkim@kaeri.re.kr

2. Experimental

The chemical composition of commercially available austenitic stainless steel Type 304H containing about 5% δ ferrite used in this work is shown in TABLE 1. The as-received material was free from sensitization because it was water quenched at mill annealing temperature. The as received material was 20% cold-rolled at room temperature to simulate strain-hardening during welding, machining or repair. Yield strength, tensile strength and elongation to rupture of the 20% cold worked material at room temperature were 745 MPa, 987 MPa and 49.7%, respectively. CT specimens were made from the cold rolled material in accordance with the ASTM E399 standard [16]. A fatigue precrack grew about 2 mm from the notch tip on the plane perpendicular to the loading direction in air and then 50 um at each loading frequency of 2×10^{-2}, 10^{-2}, 10^{-3} and 10^{-4} Hz in a SCC test solution of 325°C. The fatigue precracking path in the SCC test solution was not straight as that in air. The stress intensity maximum (Kmax.) was 30 MPam$^{1/2}$ and the ratio of the minimum load to the maximum load (R) was 0.5 during fatigue pre-cracking in air and the SCC test solution. The stress intensity maximum (Kmax.) was kept constant during fatigue cracking by decreasing the load as the crack length increased. The SCC tests were conducted at 325°C in primary water containing 1200 ppm B as H_3BO_3 and 2.2 ppm Li as LiOH with a dissolved oxygen (DO) content of 2 ppm. The load on CT specimen was kept constant during the SCC test, so the stress intensity (K) increased from 30 MPam$^{1/2}$ at the beginning of the SCC test to 32 MPam$^{1/2}$ at the end of the SCC test as the crack length increased from 12.4 to 14.4 mm during the SCC test. Even though the oxygen content in primary water is usually less than 5 ppb in the power operation stage, the SCC test was performed at a higher oxygen content in this work to simulate water chemistry in the occluded zone at the upper head of the reactor.

TABLE 1

Chemical composition of Type 304 H stainless steel (wt.%)

C	Mn	P	S	Si	Cr	Ni	N	Fe
0.056	0.76	0.025	0.012	0.41	18.13	8.25	0.048	Bal.

The CT specimen was split to 3 pieces by cutting at 1/4 and 1/2 thickness of the CT specimen after the SCC test. The crack length was measured with an optical microscope at the side surface of the two 1/4 thickness specimens after they were ground and polished. One 1/2 thickness specimen was disintegrated into 2 pieces by fatigue to observe the SCC fracture surface. The fracture surface and side surface were examined with SEM and EBSD.

3. Results and discussion

Fig. 1 shows the features around the crack at the side surface, where (a) is the band contrast image; (b) the inverse pole figure; (c) the Kernel average misorientation; and (d) the phase map. All fatigue precracking was performed at Kmax = 30 MPam$^{1/2}$ and $R = 0.5$. Fatigue precracking was applied to transit cracking path from the transgranular cracking mode to the interganular mode because many studies reported that SCC of 20% stainless steel in primary water propagates in the IGSCC mode [4]. However, in this study, SCC propagated mostly in the TGSCC mode and rarely in the IGSCC mode as shown in Fig. 1(b). The cracking mode at the crack tip region with a red rectangle in Fig. 1(a) was
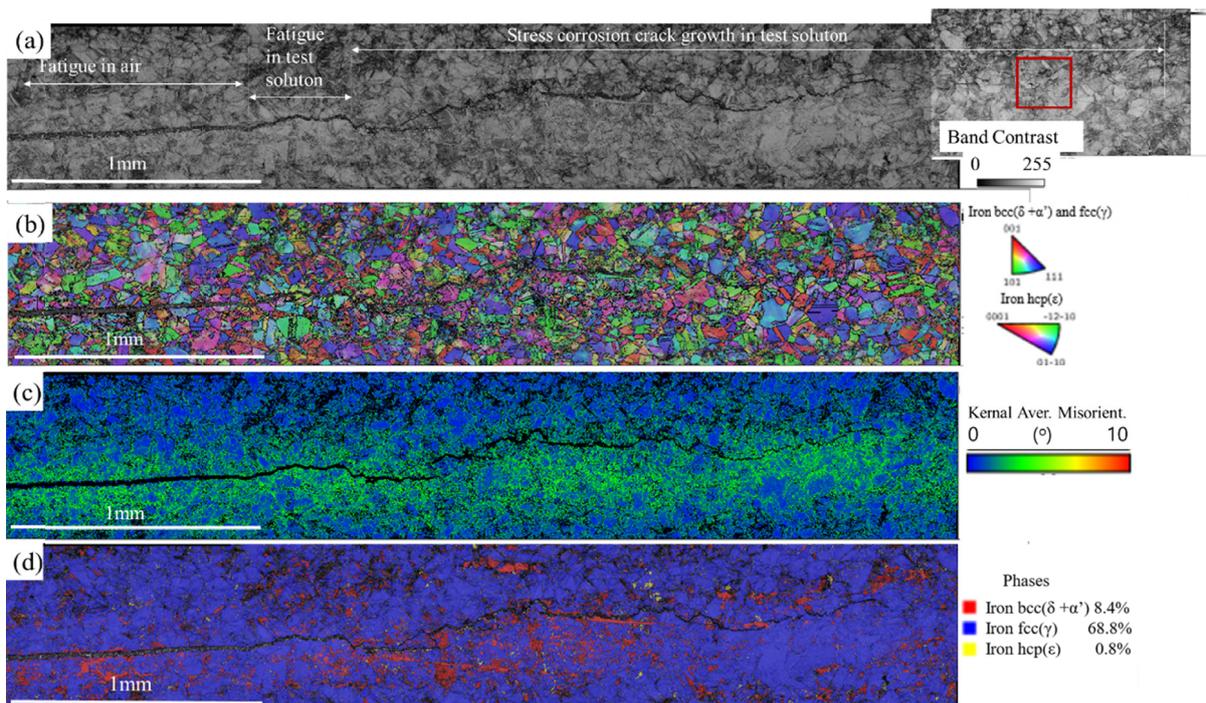
Fig. 1. Crack at the side surface: (a) Band contrast image, (b) Inverse pole figure, (c) Kernel average misorientation and (d) Phase map

examined in detail in Fig. 2. Fig. 1(c) shows that plastic deformation around the crack was produced by the applied load during the SCC test. The plastic zone size r_p, measured in Fig. 1(b) was about 0.2 mm. That, given by $r_p = 1/6\pi \times (K/\sigma_y)^2$ in plane strain condition where σ_y is yield strength, was calculated to be 0.1 mm. The plastic zone size measured in Fig. 1(c) deviated from that calculated probably because the 1/2 T CT specimen used in this work was not in the plane strain condition. Fig. 1(d) shows that phases of the 20% cold worked specimen are composed of austenite (blue), δ-ferrite (red) α' martensite (red) and ε martensite(yellow). δ-ferrite and α' martensite are not discernible with the crystal structure so they were marked red in the image. However, δ-ferrite and α' martensite are discernible by their shape. δ-ferrite is rather thick while α' martensite has a sharp line. In addition, δ-ferrite is elongated but has no relationship with slip plane while α' martensite is formed on slip plane and it looks like elongated along slip plane. Most of the deformation induced martensite is α' martensite. Both α' martensite and ε martensite were produced on the {111}plane of austenite. The presence of martensite may not affect TGSCC susceptibility because the TGSCC path was not related to the (111) plane with martensite.

Fig. 2 shows the features around the crack tip at the side surface of the CT specimen, where (a) is the SEM image; (b) the phase with the band contrast image; (c) the inverse pole figure with the band contrast image with; and (d) duplication of (a) with superposition of the cracking path. The SCC crack in grain A of Fig. 2(a) propagates in a zigzag mode. Most of the deformation induced martensite is α' martenistes that are aligned along the slip plane as shown in grain A of Fig. 2(b) and ε martensite in grain C of Fig. 2(b) is also aligned along the slip plane as α' martenistes. Slip lines are overally straight in a macroscale but slightly curved in a microscale, especially in grain C of Fig. 2(b) because of the 20% cold work. Slip lines parallel to the red line and green line in grain A of Fig. 2(c) are well distinguished by both the band

contrast image and the martensite formed on the slip lines. The slip line parallel to the blue line in grain A of Fig. 2(c) is also identified by a faint band contrast while deformation induced martensite on the slip line parallel to the blue line is not visible because the amount of deformation on the slip plane parallel blue line is less than the slip planes parallel to the red line or green line. The fourth slip plane of grain A in Fig. 2(c) was identified by a pole figure. The Pole figure of grain A shows that the fourth slip plane normal in grain A of Fig. 2(c) is almost perpendicular to the loading axis, so trace of slip line of the fourth slip plane is implicit in Fig. 2(c) because the resolved shear stress on the fourth slip plane is almost zero. In the FCC crystal structure, there are four slip planes and three slip directions on each slip plane and therefore 12 slip systems. Slip planes can be identified from the band contrast image but slip directions can not be identified from that. The amount of deformation on the slip plane is proportional to the Schmid factor. By comparing Figs. 2(a), (b) and (c), the cracking mode was marked in Fig. 2(d), where cracks in both the white elliptical circle in grain A and the green elliptical circle in grain C propagated in the transgranular mode while the crack in the red elliptical circle between grain A and grain B propagated in the intergranular mode. Cracks marked with the same color in the white elliptical circle are in the same {111} plane in Fig. 2(d). The crack in the white elliptical circle seems to have the strongest tendency to propagate along the red {111} plane and then along the green {111} plane and least along the blue {111} plane. The crack along the fourth slip plane in Fig. 2(c) was not observed because there was no slip on that plane and very low tensile stress on that plane.

Fractography near the SC crack tip (Fig. 3) shows that the crack propagated mostly in the TGSCC mode. The cracking planes marked A, B and C appear to be parallel to each other and the interfaces between two cracking planes are straight, suggesting that TGSCC has crystallographic features. By comparing Fig. 2(d)
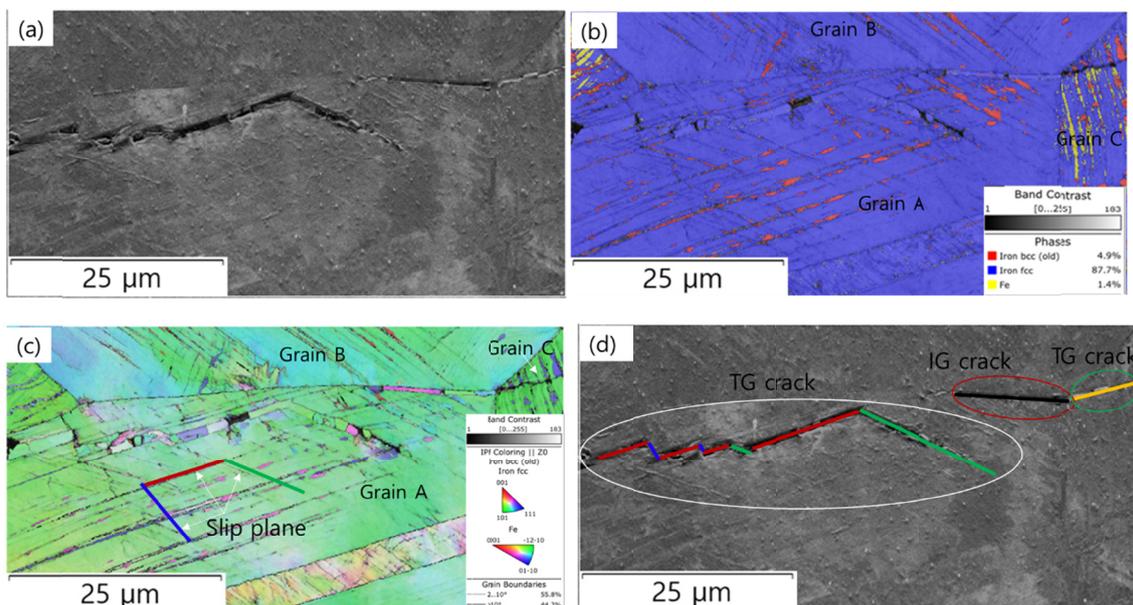
Fig. 2. Enlarged view of the crack tip at the side surface: (a) SEM image, (b) Phase with band contrast, (c) Inverse pole figure with band contrast and (d) Superposition of the cracking path on the SEM image of (a)

52
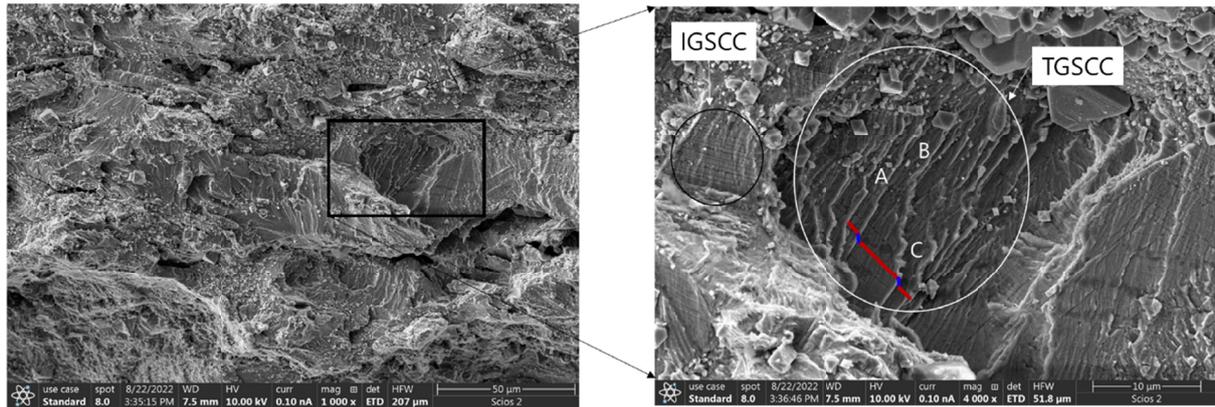
Fig. 3. Fracture surface at the crack tip region showing TGSCC and IGSCC

and Fig. 3, we can surmise that the red and blue lines in Fig. 3 correspond to those in Fig. 2(d). Therefore, the cracking planes A, B, C in Fig. 3 may be on the {111} plane. The step between two cracking planes marked by the blue line in Fig. 3 may be another {111}. The boundary between the red and blue lines is a river line.

The TGSCC paths seem to be along the {111} plane with both high resolved shear stress and high resolved tensile stress because pure shear stress does not induce SCC and the slip plane with no resolved tensile stress is immune to TGSCC. TGSCC propagated along at least two {111} planes. River lines between the two {111} planes on the TGSCC fracture surface indicating the crack propagation direction were observed. IGSCC preferentially propagated along the grain boundary perpendicular to the loading axis. The findings in this work suggest that TGSCC proceeds through formation of the weakening zone of the head of the crack tip by interaction of slip and corrosion and then cracking of the weakened zone by tensile stress. The corrosion product with an octahedron shape is spinel oxide. The EBSD technique was a very useful tool in identifying the cracking path in this work.

4. Conclusions

In this study, stress corrosion cracks propagated mostly in the TGSCC mode and sometimes in the IGSCC mode. TGSCC paths were along the {111} plane with both high resolved shear stress and high resolved tensile stress. IGSCC preferentially propagated along the grain boundary perpendicular to the loading axis. The findings in this work suggest that TGSCC proceeds through formation of a weakening zone at the head of the crack tip by interaction of slip and corrosion and then cracking of the weakened zone by tensile stress.

REFERENCES

[1] M.L.R. Ickes, J. McKinley, J.-K. Lee, J.M. Smith, A.M. Ruminski, M.A. Burke, Journal of Nuclear Materials **536**, 152 (2020).

[2] N. Huin, O. Calonne, S. Berger, B. Devrient, R. Kilian, L. Fournier, A. Marion. 17th International Conference on Environmental Degradation of Materials in Nuclear Power Systems – Water Reactors, Ottawa, Canada (2015)

[3] G.O. Ilevbare, F. Cattant, N.K. Peat, SCC of Stainless Steels under PWR service conditions. Proceedings of International Symposium Fontevraud 7, Avignon, France (2010).

[4] P.L. Andresen, Understanding and mitigating aging innuclear power plants, Woodhead Publishing, p. 236 (2010).

[5] D. Dua, K. Chen, H. Lu, L. Zhang, X. Shi, X. Xu, P.L. Andresen, Corrosion Science **110**, 134 (2016).

[6] M.O. Speidel, R. Magdowski, 11th International Conference on Environmental Degradation of Materials in Nuclear Power Systems – Water Reactors, Newport Beach California, p. 325 (1999).

[7] R. Bakish, Trans. AIME **209**, 494 (1957).

[8] T.B. Cassagne, W.F. Flanagan, B. D. Lichter, Metall. Trans. A **17**, 703 (1986).

[9] J.I. Dickson, D. Groulx, L. Shiqong, Materials Science and Engineering **94**, 155 (1987).

[10] Mukai, Y. Mukai, M. Watanabe, M. Murata, ASTM STP **645**, 164 (1978).

[11] E.I. Meletis, R.F. Hochmann, Corros. Sci. **24**, 843 (1984).

[12] E.I. Meletis, R.F. Hochmann, J. Testing Eval. **142**. 12, 142 (1984).

[13] R. Liu, N. Narita, C. Altstetter, H. Birnbaum , E. N. Pugh, Metall. Trans. A **11**, 1563 (1980).

[14] T. Nakayama, M. Takano, Corrosion **37**, 229 (1981).

[15] S.Y. Chang, S.T.Oh, M.J. Suk, C.S. Hong, J. Kor. Powd. Met. Inst. **21**. 2, 97 (2014).

[16] ASTM Standard E 399, ASTM International, PA, (2007).